# 3D mesoscale finite element modelling of concrete

# 3D Mesoscale Finite Element Modelling of Concrete

Rongxin Zhou, Zhenhuan Song, Yong Lu*

Institute for Infrastructure and Environment, School of Engineering, The University of Edinburgh, Edinburgh EH9 3JL, UK

* Correspondence: yong.lu@ed.ac.uk

**Abstract**

Concrete is non-homogeneous and is composed of three main constituent phases from a mesoscopic viewpoint, namely aggregates, mortar matrix, and interface transition zone (ITZ). A mesoscale model with explicit representation of the three distinctive phases is needed for investigation into the damage processes underlying the macroscopic behaviour of the composite material. This paper presents a full 3-D mesoscale finite element model for concrete. On top of the conventional take-and-place method, an additional process of creating supplementary aggregates is developed to overcome the low packing density problem associated with the take-and-place procedure. An advanced FE meshing solver is employed to mesh the highly unstructured domains. 3D mesoscale numerical simulation is then conducted for concrete specimen under different loading conditions, including dynamic loading with high strain rate. The results demonstrate that detailed mesoscopic damage processes can be realistically captured by the 3D mesoscale model while the macroscopic behaviour compares well with experimental observations under various stress conditions. The well-known inertial confinement effect under dynamic compression can be fully represented with the 3D mesoscale model and the trend of dynamic strength increase with strain rate from the 3D mesoscale analysis agrees well with the experimental data.

Keywords: concrete; heterogeneity; 3D mesoscale model; micromechanical damage; failure mechanism; dynamic compression

# 1. Introduction

Concrete is the most widely used construction material in the world. It has a great variety of applications in the field of structural engineering. However concrete is a highly non-homogenous material with large heterogeneities. The damage and failure process of concrete depends closely on the material composition and the interaction between different constituent phases; for example it is well known that the initiation of macroscopic damage generally starts from the fracture along the interfaces between aggregates and the mortar matrix (the so-called interface transition zone, or ITZ). The extent to which the heterogeneity should be described in a computational model would depend upon the level (scale) of observation and the stress-strain conditions particularly the gradient involved in the problem.

Generally speaking, modelling of concrete may be classified into three distinctive scales namely macroscale, mesoscale and microscale. On the macroscale, concrete is traditionally considered as homogeneous material and treated as such in classical finite element models. Strictly speaking, the treatment of concrete as a homogeneous solid is only valid when macroscopic scale of observation is of interest and the stress-strain variation in critical regions is not drastic [1]. On the mesoscale, concrete is considered as a composite material comprising of coarse aggregate, mortar matrix and the interfacial transition zone (ITZ). An explicit mesoscale model permits a direct description of the material heterogeneity and hence has the ability to allow for a realistic prediction of the development of damage within the muti-phase material. At the microscopic level, the mortar matrix of the previous level is further divided into fine aggregate and hardened cement paste with pores embedded inside. As far as the composite mechanical behaviour is concerned, subdivision within each individual phase does not appear to introduce significant effects [2]. Therefore modelling of concrete on a mesoscale is deemed to be the most practical and useful choice when material heterogeneity needs to be taken into account. Example applications where such a need arises include investigation into concrete damage and fracture mechanisms under complex stress conditions, concrete response under high strain rates, and fracture and aggregate interlocking mechanisms in critical zones of a concrete member.

A number of studies on mesoscale modelling of concrete using a continuum approach can be found in the existing literature [3-22]. Relatively more realistic aggregate shapes, such as random polygon, have been achieved mainly in 2D (e.g. [3-7]). However, a 2D mesoscale model has inherent limitation in representing a realistic stress and strain condition in concrete

specimen, particularly when pressure and confining stress becomes important such as in dynamic compression where lateral inertial confining effect is deemed a critical factor.

Most of the existing mesoscale modelling studies in 3D have adopted simple shapes of aggregate particles like spheres [8, 9] or mixed spheres and ellipsoids [10] to circumvent the difficulty of creating random aggregate shapes. A modified version of the ellipsoid function [11] made it possible to better approximate real aggregates. Approximation of particle shapes by polyhedrons generated from Voronoi tessellation point set has been adopted by some researchers [12-15]. This method can capture the real aggregate shape better than simple spheres and ellipsoids but it is difficult to satisfy the pre-defined aggregate size grading curve. Some more recent studies have focused on developing approaches which can generate and randomly pack polyhedron aggregates following a predefined grading curve [16-18]. However, a common challenge to most existing meso-structure models of concrete is a relatively low aggregate packing density and it is generally difficult to reach the aggregate volume ratio as in the real concrete specimens. It is worth noting that in some studies where higher volume fractions of aggregates have been reported (e.g. [19, 20]), those were not the real packing densities for the polyhedron aggregates but the equivalent spherical particles.

In a different approach, direct mapping of the aggregate particle from physical samples has been explored using computer image analysis and computed tomography (CT-scan) [21-24]. However, the major limitation of this technique is that it would be very time-consuming and expensive to obtain meaningful analyses by preparing, fabricating, cutting specimens and then dealing with the scanned images.

In an effort to develop a comprehensive mesoscale model for concrete, a series of studies has been conducted in this research group. The model is aimed at achieving a realistic representation of the actual shapes and sizes of aggregate particles and at the same time allowing for high volumetric ratios of aggregates to be attained. The work reported in this paper is concerned about a full 3D mesoscale model. In the proposed approach, 3D polyhedral-shaped aggregates are represented by convex hull in $R^3$, which is the minimum convex set containing a series of points generated randomly. Gravel and crushed shapes of polytopes are both considered to enable greater flexibility in the simulation of real shapes of aggregate particles. The standard take-and-place procedure is used for generating the main 3D meso-structure. Extending from a basic framework [16], the present study focuses on improving the efficiency in the generation of the 3D mesoscale geometry and the robustness of finite element meshing for the highly unstructured mesoscale model, as well as enabling the realisation of high density

packing of aggregates. The mesoscale model generated from the enhanced procedure is verified against standard experimental observations under quasi-static compression and tension. The model is then further applied to simulate the dynamic behaviour of concrete under high strain rate compression.

## 2. Generation of the 3D mesoscale geometric structure

Similar to the generation of the 2D mesoscale model, the classical 'Take-and-Place' procedure [6] is used to generate the 3D meso-structure in the first step. The 'Take' process generates an individual aggregate (polytope) through a random sampling operation in terms of the size and the shape parameters. The 'place' process subsequently places the aggregate into the predefined 3D specimen space, satisfying geometric constraints including no-intersection with other aggregates and the specimen boundaries. The whole process is executed in a sequential manner controlled by the target aggregate volume ratio, starting with the largest aggregate size group, and carrying on until the smallest size group is completed. The generation of 3D meso-structure is implemented in MATLAB.

### 2.1. Aggregate size distribution

In normal concrete, the coarse aggregate is defined to consist of particles having a nominal size greater than 4.75 mm [9]. For normal concrete the coarse aggregates take up around 40-50% of the mixture volume. The particle size distribution for aggregate is usually defined by a grading curve. Herein we adopt a standard Fuller grading curve, which can be expressed as:

$$P(d) = 100 \times \left(d / d_{\max}\right)^n \tag{1}$$

where $P$ is the cumulative volume percentage of aggregates below size $d$, $d_{max}$ is the maximum size of the aggregates. The exponent $n$ is normally in the range of 0.45-0.70. Herein $n$ is assumed to be 0.5. Thus the volume ratio of aggregate within each grading segment $[d_s, d_{s+1}]$ can be calculated as [9]:

$$V_R[d_s, d_{s+1}] = \frac{V_{agg}[d_s, d_{s+1}]}{V_s} = \frac{P(d_{s+1}) - P(d_s)}{P(d_{\max}) - P(d_{\min})} \times v_p \tag{2}$$

where $V_{agg}[d_s, d_{s+1}]$ is the volume of aggregate within the discretized aggregate size range $[d_s, d_{s+1}]$. $P(d_i)$ can be calculated from Eq. (1) provided the aggregate size is given. $v_p$ is the

total amount volume percentage of aggregate in concrete and $V_s$ is the volume of concrete specimen. $d_{max}$ , $d_{min}$ are the maximum and minimum coarse aggregate particle size.

The basic reference case of concrete considered herein is the type of medium aggregates with the coarse aggregates varying in size between 4 to 12 mm. For simplicity the aggregates are divided into four size intervals, namely, 4-6 mm, 6-8 mm, 8-10 mm, and 10-12 mm. For a coarse aggregate volume ratio of 45%, which is the target volume ratio to be achieved in the 3D mesoscale model, the percentages of the above four aggregate groups will be 14%, 12%, 10%, and 9% respectively.

It should be noted that the procedure itself has no restriction on the aggregate size range or its distribution. The number of intervals for the whole size range is also not restrictive. Furthermore, as will be discussed later, within each of the 4 size intervals considered herein, for example 4-6 mm, the size of an individual aggregate still varies randomly according to a uniform distribution within the interval. This effectively results in a linear increase in the cumulative grading curve between 4 mm and 6 mm, which is deemed to be good enough to represent an actual curve within a size interval.

## 2.2. Individual aggregate particle generation

In an actual concrete specimen, the aggregate shape and surface texture can be classified as rounded, angular or polyhedral. Highly irregular particles can also have flaky and elongated shape. In this study, polyhedron-shaped aggregates are considered. Other special shapes, such as round or ellipsoid, are relatively simple to generate, and they may also be approximated by polyhedrons with specially chosen shape parameters.

One classical approach to describe the shapes of gravel aggregates mathematically is based on the morphological analysis. In 2D, the shape of a gravel aggregate can be characterised by transforming the boundary contour of each particle into polar coordinates. Thus the trace of an aggregate can be expressed with the polar radius $r$ as a Fourier series (i.e. harmonic function) of the polar angle $\theta$ [25]:

$$r(\theta) = r_0 + \sum_{m=1}^{\infty} A_m(\cos m\theta + \varphi_m) \qquad (3)$$

where $r_0$ is the average radius. The term $\sum_{m=1}^{\infty} A_m(cosm\theta + \varphi_m)$ characterises the particle contour where $A_m$ are the amplitudes of the Fourier frequencies with the corresponding whose phase angles $\varphi_m$ and $m$ are the harmonic numbers. According to the morphological law

proposed by Beddow and Meloy [25], there should be a linear relation between log($A_m$) and log($m$):

$$\log(A_m) = a\log(m) + b \tag{4}$$

where $a$ and $b$ are parameters characterizing the shape of the set of particles. Thus numerically the shape of a gravel particle may be approximated by a series of short straight line segments in 2D [6]. An inscribed polygon of circle can then be used to represent the relatively regular aggregate while an elongation and shrinking procedure can be applied on it to produce elongated and flaky aggregate.

This idea can be extended to 3D case, where the spherical harmonic mathematical analysis is used to characterise the boundary of a real aggregate [26]. Similarly regular aggregates can be represented by inscribed polyhedrons of spheres while un-regular aggregates can be produced by applying elongation and shrinking procedure as is done in 2D case.

*a) Regular aggregates*

As is stated above, an inscribed polyhedrons of sphere is used to characterise the real shape of regular aggregate. Thus the generation process starts from picking a set of random points on the surfaces of the spheres. These random points can be expressed as the following equations using spherical coordinates by radius $r_0$, inclination angle $\theta$, azimuth angle $\varphi$:

$$R_{ix} = r_0 \sin\theta\cos\varphi \tag{5a}$$

$$R_{iy} = r_0 \sin\theta\sin\varphi \tag{5b}$$

$$R_{iz} = r_0 \cos\theta \tag{5c}$$

It is worth noting that variables $r_0, \theta$ and $\varphi$ are random numbers from a uniform distribution. Thus we can have:

$$r_0 = \frac{1}{2}\times\left[d_1 + \lambda\times(d_2 - d_1)\right] \tag{6a}$$

$$\theta = \gamma\times 2\pi \tag{6b}$$

$$\varphi = \chi\times 2\pi \tag{6c}$$

where $d_1$ and $d_2$ are the minimum and maximum diameters for each segment in the size distribution, $\lambda, \gamma, \chi$ are three independent random numbers uniformly distributed between 0 and 1. The points used to generate the polytope also have random numbers $n$, which may significantly influence the shape of an aggregate. Generally a larger number of points make it

possible to generate gravel shape aggregate while small number of point produce angular shape aggregate. This will be shown later.

After picking a series of random points as specified above, we create the aggregate particles by bounded polyhedrons. The convex hull for a set of points is the minimum convex polyhedron containing all the predefined points [27]. Thus it is possible to generate a random shaped aggregate particle from a set of 3D random points. The convexity of the polyhedron can be automatically fulfilled without separate checking at every step. Fig. 1 gives an example of a convex hull generated using Matlab with a computational geometry function named Qhull.

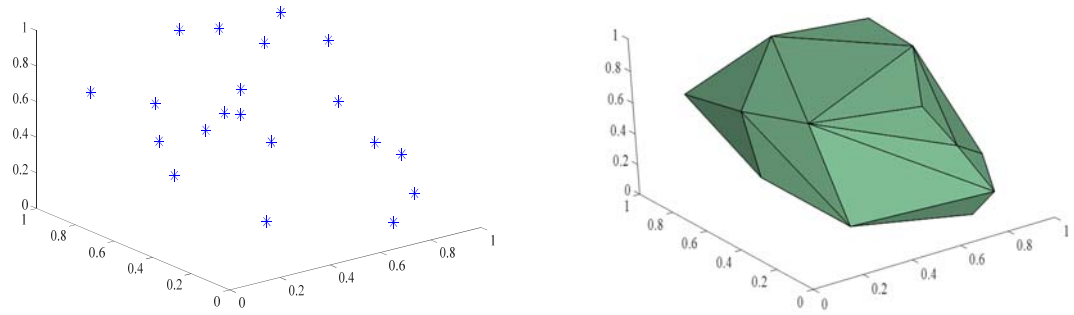

Fig. 1. An example convex Hull. Left = random points; right = generated convex hull

*b) Crushed aggregates*

The shapes of aggregate particles created above are inscribed polyhedrons of sphere which are relatively regular. Both flaky and elongated aggregates can be realised from the regular polytopes by shrinking or elongation. A flaky shape is implemented by introducing a random shrinkage ratio *s* (*s*<1) on one dimension but expanding the other dimensions simultaneously, and to keep the nominal volume of the aggregate unchanged we have:

$$R'_{ix} = s \times R_{ix} \tag{7a}$$

$$R'_{iy} = R_{iy} / \sqrt{s} \tag{7b}$$

$$R'_{iz} = R_{iz} / \sqrt{s} \tag{7c}$$

where ($R_{ix}$, $R_{iy}$, $R_{iz}$) is the original coordinate for the $i^{th}$ vertex on a regular polytope while $(R'_{ix}, R'_{iy}, R'_{iz})$ is the transformed one.

An elongated shape will result if an expansion ratio *s* (*s*>1) is employed.

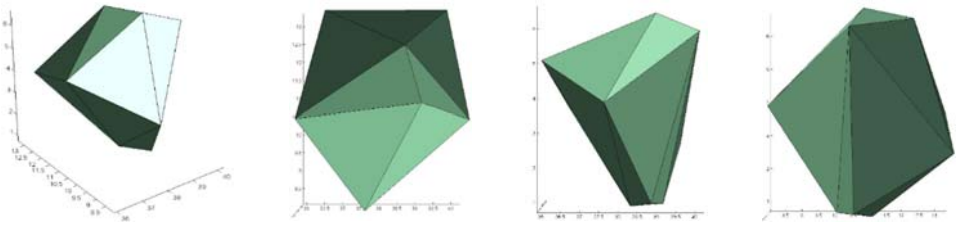

Global view X-Y view X-Z view Y-Z view

(a) Polytopes with 10 random points

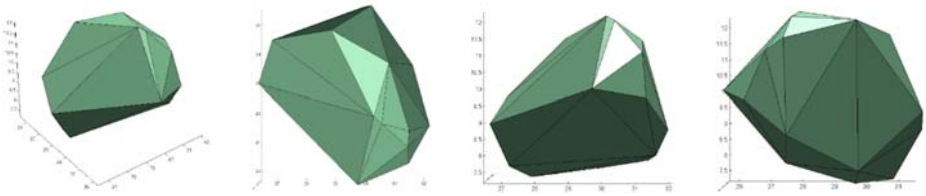

Global view X-Y view X-Z view Y-Z view

(b) Polytopes with 20 random points

Fig. 2. Sample polytopes shape with different number of random points

In summary a series of random parameters (five in total i.e. $n, \lambda, \gamma, \chi$ and $s$) are required to produce an arbitrary shape of 3D aggregate particle. As shown in the Fig. 2, the polytope with only 10 random points has clear angular edges and corners, and with increase of the random points the shape of the polyhedron becomes smoother. Considering the actual aggregate shapes and a balanced computing time, the number of random points used to create the polytopes is controlled between 15 and 25 in the present study. Shrinking and elongation can the then be performed to create elongated and flaky particles, as shown in Fig. 3.

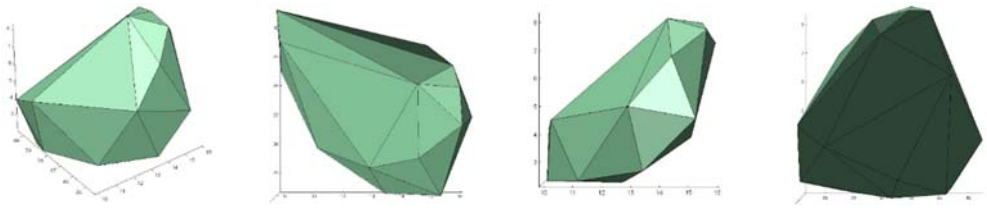

Global view X-Y view X-Z view Y-Z view

(a) $s$ = 0.5

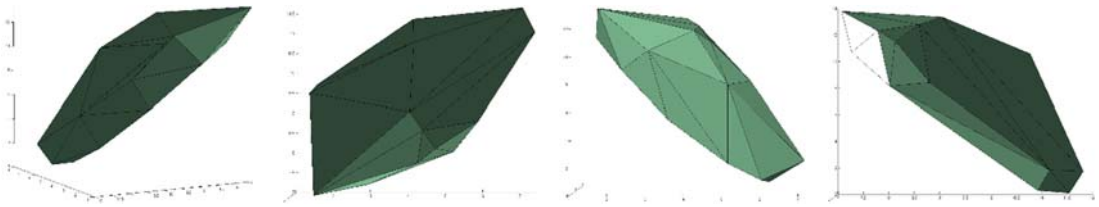

Global view X-Y view X-Z view Y-Z view

(b) s = 3

Fig. 3. Examples of flaky and elongated particles generation with 20 random points.

## 2.3. Placing particles

After generating an individual aggregate particle, the 'place' process is carried out to place the particle into the predefined sample space in a random manner, subjected to prescribed physical constraints.

The most important and time consuming step in the placing process is the intersection checking between two polytopes. Two obvious conditions should be satisfied. Firstly the whole polytope should be completely within the boundary of the concrete specimen; this can be ensured relatively easily by making sure all of the random points which have been used to form the vertices of the polytope are within the boundary of the defined space. Secondly there should not be any intersection with any existing (already placed) aggregates. The check of this condition would require much more intensive computation in 3D modelling. To increase the check efficiency, only the neighbouring aggregates need be checked, and this is done in two steps. The first step is to identify the neighbouring aggregates which may have a chance to intersect with the new aggregate. At this step the new aggregate, as well as the existing ones, is represented by a bounding sphere which shares the same centre point as the convex hull and covers all vertices of the polytope, as illustrated in Fig. 4. Any aggregate which has the distance of its centre to the centre of the new aggregate to be smaller than the sum of the radii of the two spheres is picked out as candidates of intersection. In the second step, a more detailed check is carried out on the limited number of candidate particles.

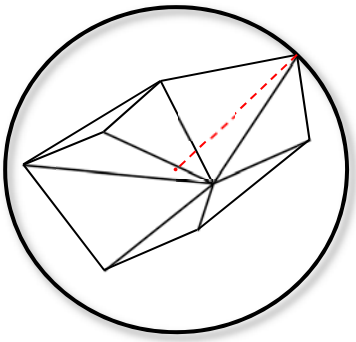

Fig. 4. Local checking space

The clipping and capping algorithm [28] is then employed to detect the intersection between the aggregate being placed and the existing particles picked out above. The algorithm is based on the concept that any 3D convex polytope can be represented by a list of plane indicating a facet (i.e. any bounded polytope in 3D can be reconstructed by the boundary surfaces in half-spaces) [27]. Then the intersection checking between two convex polytopes can be converted to the intersection of the polygonal surfaces in one polytope with the cutting planes in the other polytope. Full details of the algorithm on clipping and capping can be found in [28].

## 2.4. Enhancement on the placing of aggregates

In the standard "place" procedure, once an aggregate being placed is found to intersect with any existing aggregates, this aggregate will be abandoned and a new polytope is regenerated and placed into a new position, and the checking process is carried out all over again. In order to increase the success rate of placing the aggregate and hence improve the placing efficiency, a translate-and-rotate procedure is employed on the aggregate which is being placed, as described in the following.

The translation is done by translating the whole particle by a small distance, which is defined by three increments, $\Delta x, \Delta y, \Delta z$ , in the three axis directions respectively. Each of these incremental components is taken randomly (assuming a uniform distribution) within a small range defined by a fraction of the nominal aggregate size, both positive and negative. The translated coordinates in the Cartesian system for each vertex "*i*" of the particle are thus:

$$VP_i^{'} = (x_i + \Delta x, y_i + \Delta y, z_i + \Delta z) \qquad (8)$$

For a 50mm sample cube with nominal aggregate size of 10mm as used in the numerical simulation described later, the increment in each axis direction is taken in the range of (-1.5 to +1.5mm).

The intersection check is immediately carried out after the translation. If intersection is found to still exist, a random rotating operation is performed. According to Euler's rotation theorem, any rotation of an object in 3-dimenisonal Euclidean space can be achieved by three elemental rotations, namely $\alpha, \beta, \gamma$ with respect to $x, y$ *and* $z$ axis respectively. In the random rotating operation, these three angles are sampled independently within their variable range, i.e. -90 to +90 degrees. It should be noted that the final rotation matrix can be dependent on the sequence of the three rotations. In the present procedure the rotation is done first about the x-axis, then the y-axis, and finally the z-axis, thus:

$$T = \Gamma_z(\gamma)\Gamma_y(\beta)\Gamma_x(\alpha) \tag{9}$$

where

$$\Gamma_x(\alpha) = \begin{bmatrix} 1 & 0 & 0 \\ 0 & \cos\alpha & -\sin\alpha \\ 0 & \sin\alpha & \cos\alpha \end{bmatrix}, \Gamma_y(\beta) = \begin{bmatrix} \cos\beta & 0 & \sin\beta \\ 0 & 1 & 0 \\ -\sin\beta & 0 & \cos\beta \end{bmatrix}, \Gamma_z(\gamma) = \begin{bmatrix} \cos\gamma & -\sin\gamma & 0 \\ \sin\gamma & \cos\gamma & 0 \\ 0 & 0 & 1 \end{bmatrix} \tag{10}$$

The intersection check is carried out again after the rotation. This completes one round of translation-rotation operation and the associated check. To avoid waste of effort for a bad position, a limit number of translate-and-rotate operations can be set. From the trial analysis in the present study, a limit of 50 times appears to be adequate and the attampt will be abondoned if a valid position is still not resulted at that point.

When compared with the procedure without consideration of the translate-and-rotate method it is found that the translate-and-rotate procedure not only reduces the computing time (by about 60%) but also can result in an increase in the aggregate volume percentage (by about 4%). Despite the improvement, however, when a high volume ratio of aggregates such as 40-50% is desired the enhanced 'take-and-place' procedure would still become very time-consuming and likely to fail to achieve such high packing density. Thus an alternative approach would be needed to further increase the aggregate percentage, and this will be discussed in the next section.

# 3. Finite element meshing and generation of supplementary aggregates

## 3.1. Meshing methodology

Due to the randomly shaped aggregate particles, the meso-structure is highly unstructured. For meshing unstructured domain, triangle and tetrahedral meshing are mostly used in the grid refinement. Specific smoothing algorithms for meshing unstructured domain include Octree, advancing front and Delaunay refinement [29]. A typical way to work around the difficulty arising from meshing directly the highly unstructured mesoscale geometry has been to firstly perform a background meshing and then bundle groups of the meshed elements into aggregates of desired shapes [19, 30]. The obvious drawback of such an approach is that the actual surfaces of the aggregates cannot be preserved.

In the present mesoscale model we adopt a direct approach to meshing the mesoscale structure of concrete. An advanced meshing code, called TetGen [31], is employed to do this task. This meshing code is one type of Delaunay triangulation, and it aims to maximize the minimum angle of all the angles of a triangle in the triangulation, thus largely avoiding skinny or badly shaped triangles. A typical way in this algorithm is to generate an initial node set by meshing the boundary of the geometry. The boundary nodes are then triangulated with Delaunay triangulation. However it should be noted that not all the boundaries of the structure, especially in 3D, can conform to the Delaunay triangulation. Hence a generalization of the Delaunay triangulation called constrained Delaunay triangulation (CDT), which forces certain required segments into the triangulation, has been proposed in computational geometry literature [32]. The TetGen code, which is based on the (CDT), treats the 3D unstructured geometry to a more general input called piecewise linear complex (PLC) [33]. A PLC can be easily decomposed into a constrained Delaunay tetrahedronlization provided it has a CDT. The code successfully resolves the problem of non-existence of a CDT by updating the input PLC into another PLC which is topologically and geometrically equivalent to the original one and does have a CDT. The advantage of using this type of meshing method is that it can retain realistic boundaries between aggregate and mortar. This provides an essential basis for the simulation of stress concentration, crack initiation and damage accumulation in concrete from a mesoscopic perspective.

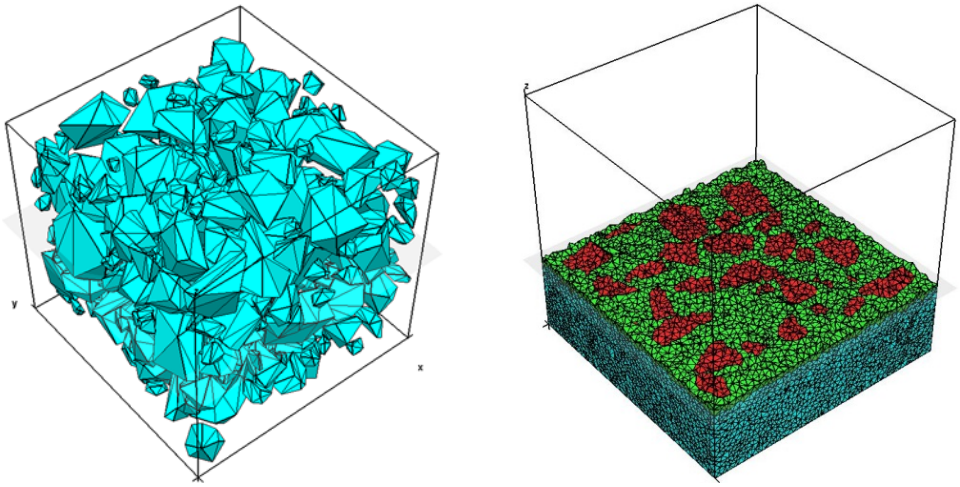

Fig. 5. 3D meso structure and mesh result

Fig. 5 and Fig. 6 show an example of the 3D structure and meshing result of a cubic concrete specimen. Note that up to this point only aggregate and mortar elements have been generated; the polytope particles represent the aggregates and the remaining domain belongs to the mortar material.

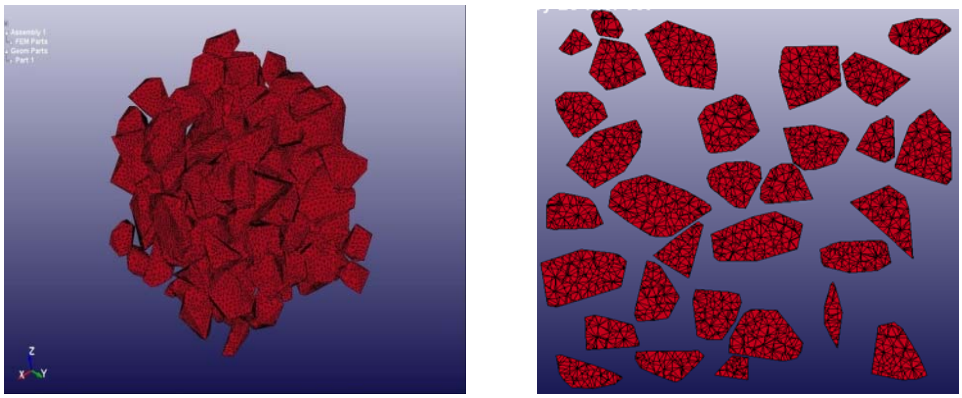

(a) Aggregates elements left = 3D view, right = a plane cut view

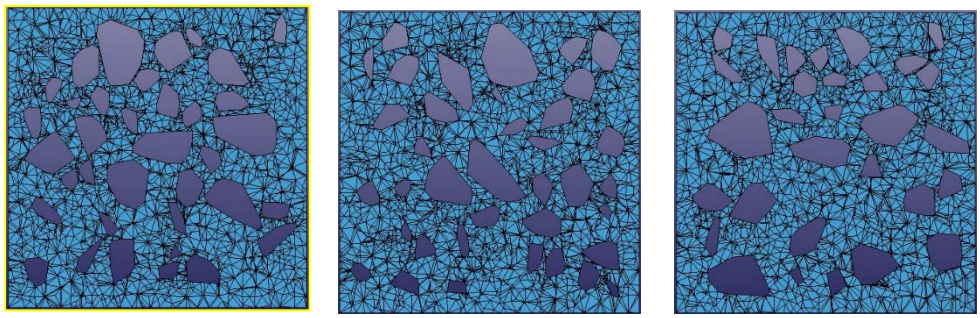

(b) Mortar elements x, y, z plane cut view respectively

Fig. 6. Meshing results for aggregates and mortar

The generation of the third phase, i.e. the ITZ can be made by different methods depending upon the way the ITZ is to be modelled, for example by "shrinking" the already formed aggregates to leave an interface layer between the aggregates and the mortar matrix which is subsequently meshed as ITZ. Using cohesive elements is another option; however, due to complex stress conditions at the mortar-aggregate interface, typical cohesive element formulation is found to exhibit poor performance in a mesoscale model [5]. In the present study we use the equivalent solid layer approach to represent the effect of ITZ.

As an alternative to shrinking aggregates, in the current scheme the equivalent ITZ layer is generated after the initial meshing of mortar domain, by choosing mortar elements that immediately come into contact with the aggregates. The procedure is straightforward and one just needs to pick up those elements in mortar domain which have shared nodes with the aggregates. This means if a mortar element shares at least one node with any aggregate, then the element will be defined as an interface element. Otherwise the element remains in the mortar domain. An in-house selection program has been developed using MATLAB to identify the layer of elements surrounding aggregate particles. Fig. 7 shows the identification results and the ITZ elements thus defined.

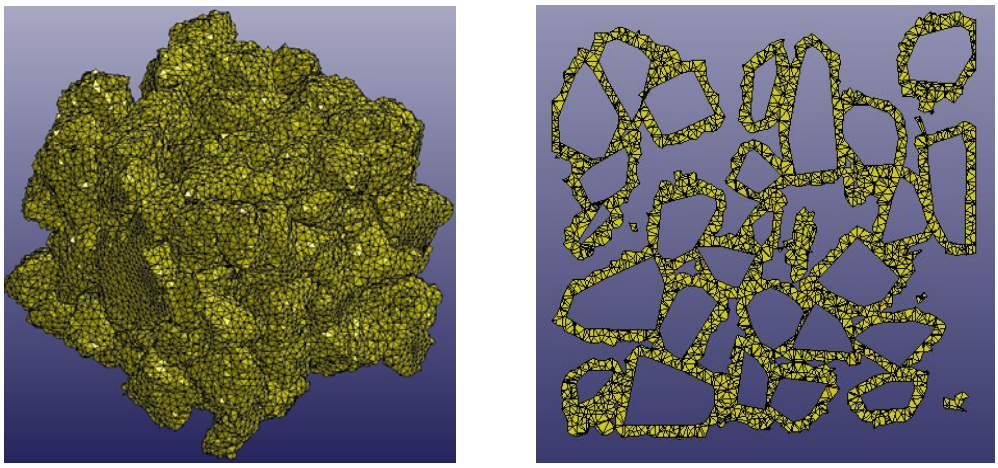

Fig. 7. ITZ layer; left = 3D view, right = a plane cut view

One may note that the ITZ defined by the above 'equivalent' solid layer will generally exhibit some degree of uneven thickness which depends on the mesh size, and it can also be rather non-smooth. The thickness issue may be dealt with in the assignment of the equivalent ITZ properties for a specific mesh size, which will be discussed further in Section 3.2.2. The effect of the non-smooth feature, on the other hand, is expected to average out over a few ITZ

elements that form a small fraction of the interface between an aggregate and the surrounding mortar elements, and therefore will not affect sensitively on the damage processes.

It is worth noting that the meshing processes for the type of concrete specimens under consideration is rather efficient, and with a standard desktop computer with dual-Intel core i7@3.4GHz and 64 GB RAM, the total running time for the meshing is on the order of 100 seconds.

## 3.2. Creation of supplementary aggregates

As has been discussed above, a practical limitation of the take-and-place method when applied in 3D meso-scale modelling is the packing density; even with the enhancement operations it is difficult to achieve an aggregate volume ratio as high as 40-50%, which is typical in normal concrete.

Based on the experiences from the present study, the maximum aggregate volume ratio that may be achieved from the standard take-and-place procedure is around 30% when the grading curve is closely followed, and with the enhanced operations described in Section 2.4 the ratio may be increased to about 35%.

To facilitate the discussion let us stay with the particular cubic concrete specimen, and we aim to generate an aggregate volume ratio of 45%. For simplicity we have subdivided the aggregates into four discretized ranges according to the Fuller curve, namely i) 4-6 mm, 14%; ii) 6-8 mm, 12%; iii) 8-10 mm, 10%; and iv) 10-12 mm, 9%. We firstly follow the standard take and place procedure and start from the largest aggregate size group (10-12 mm). We find that the volume percentage of the first two size groups, i.e. the 10-12 mm and 8-10 mm groups herein, can be perfectly completed. But for the third group 6-8 mm, the maximum aggregate ratio that can be achieved is around only 10%, and further attempt to fill in the remaining 2% can be extremely time consuming and may not succeed at all. It is still possible to pack some aggregates of the next group (4-6 mm), but only a small fraction of the target volume percentage for this group may be achieved. Clearly the missing amounts of aggregates in the two smallest size groups (6-8 mm and 4-6 mm herein) can only be generated using methods outside the take-and-place procedure.

To tackle the above difficulties we propose to proceed, upon exhausting the “take-and-place” operation, to finite element meshing and create supplementary aggregates from the meshed FE domain, such that selected mortar elements in qualified neighbourhood are grouped to form the

remaining aggregates. The neighbourhood is identified by a virtual sphere whose diameter matches the nominal size of the aggregates to be created. The positioning of the sphere is random but a valid position should have the sphere meeting a similar set of criteria as an aggregate in the normal take-and-place procedure, namely no intersection or overlapping with any existing aggregates. In this sense the general effect of such a procedure to generate the supplementary aggregates is analogous to the take-and-place procedure.

The operation is controlled by the balance of the aggregate volume ratio for each segment size group, which means the secondary aggregates are formed one by one until the target aggregate volume ratio is fulfilled.

For each size group requiring the generation of the supplementary aggregates, a virtual sphere of nominal diameter equal to the upper-end size in the size group, $d_2$, is employed to encircle a target space for a new aggregate. For example $d_2$ = 8 mm for the 6-8 mm group. The process can then be subdivided into two main steps:

Step 1: Placing the centre of such a virtual sphere into the mortar space in a random manner. Considering that by this stage all mortar elements have been meshed and a library can be created to contain all mortar elements with their respective nodal coordinates, placing the virtual sphere can be effectively done by putting its centre to the centroid of a mortar element at random. A checking process then proceeds to see if the location of the sphere is a valid one with no intersection with other aggregates and the boundary.

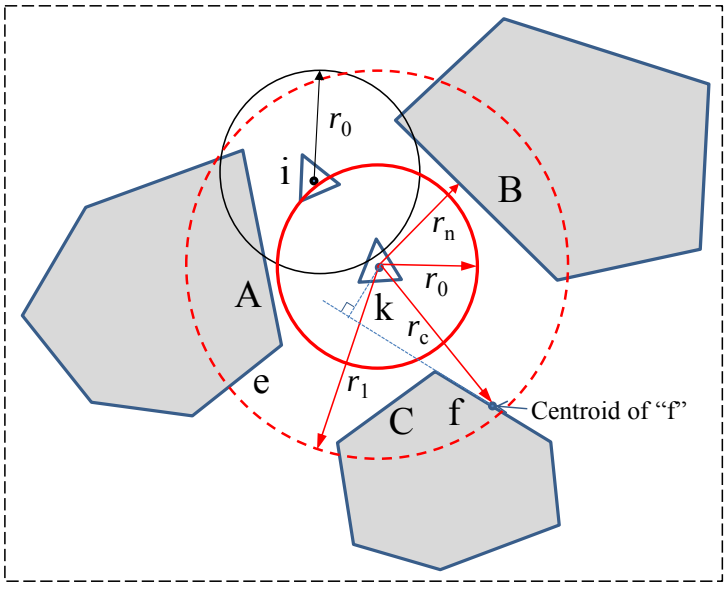


Fig. 8. Schematic of placing the virtual sphere and intersection checking

Step 2: After the base mortar element (centre of the sphere) is successfully selected from the above step, the new aggregate grouping process and the new ITZ identifying process can be carried out with respect to the virtual spherical space.

Fig. 8 illustrates schematically the relative position of a virtual sphere in the mortar domain, where "i", "k" denotes a random mortar element, respectively, to which a trial sphere is placed. For illustration purpose, "i" indicates an invalid base element while "k" represents a valid base element.

Understandingly a proper location of the base element and a suitable grouping process are equally important in determining an adequately shaped secondary aggregate. Discussions on these two topics in detail are given in the following seb-sections. The general procedure for creating secondary aggregates is programmed using MATLAB code.

*3.2.1. Base element*

As stated above it is important to choose a proper location for the base mortar element because it is essentially the centre of the virtual sphere for the formation of a supplementary aggregate and will therefore significantly influence the shape of the secondary aggregate. A valid base mortar element should satisfy the following three conditions:

1. It should not result in any overlapping or intersection between any two supplementary aggregates.
2. The base element should be kept at a certain distance away from the boundary surfaces of the specimen, such that the virtual sphere does not intersect the boundary surfaces.
3. The base element should have a minimum distance from the surfaces or edges of the surrounding aggregates (polytopes) created in the first batch with the 'take-and-place' procedure.

Condition 1 can be satisfied by checking the distance between the base element and any previously selected base elements (stored in a valid base elements array $VB_k(x_k, y_k, z_k)$, where $k$ is the order number of the valid base element and $(x_k, y_k, z_k)$ is its centroid coordinates), such that

$$\delta_k \geq 0.5(d_2 + d_p) \tag{11}$$

where $d_2$ is the diameter of the current virtual sphere, and $d_p$ is the diameter of the virtual sphere for an already formed supplementary aggregate.

Condition 2 can be satisfied by checking the distance from the base element to any of the boundary surfaces. This distance by default should be greater than the radius of the virtual sphere. For a cubic or prismatic specimen, this condition may be implemented more efficiently by creating a reduced specimen space by shrinking all sides by the same margin (equal to the radius of the virtual sphere), and checking that the base element falls within the shrunk space.

Condition 3 is checked after meeting the first two conditions. The procedure is not straightforward and involves several considerations, as detailed below.

a) The primary check is the normal distance from the base element to the surfaces of an existing aggregate polytope, i.e. the distance $r_n$ shown in Fig. 8. The centroid point for each candidate base element is available after the meshing (herein from the post-processor LS-PREPOST 4.2). Its normal distance to a surface of a polytope can be calculated using the following formula:

$$|r_n| = \frac{|ax_0 + by_0 + cz_0 + d|}{\sqrt{a^2 + b^2 + c^2}} \tag{12}$$

where point $CP_0 = (x_0, y_0, z_0)$ represents the centroid of the base element, and the plane representing a surface of a polytope being checked is $ax + by + cz + d = 0$.

Geometric data generated in the Take-and-Place procedure are processed to establish the planes for all the surfaces of an aggregate polytope. These geometric data include the coordinates of all the vertex points, and the three co-planar vertex points for each surface of the polytope. These data are extracted from the output of the convex hull generation procedure in MATLAB described in Section 2.2.

Let the three vertex points on a surface of a polytope be $A(x_1, y_1, z_1)$, $B(x_2, y_2, z_2)$ and $C(x_3, y_3, z_3)$, the normal vector of the surface can be obtained as:

$$\vec{n} = \overrightarrow{AB} \times \overrightarrow{AC} = \begin{vmatrix} \vec{i} & \vec{j} & \vec{k} \\ x_2 - x_1 & y_2 - y_1 & z_2 - z_1 \\ x_3 - x_1 & y_3 - y_1 & z_3 - z_1 \end{vmatrix} = a\vec{i} + b\vec{j} + c\vec{k} \tag{13}$$

The equation for the plane is therefore:

$$a(x - x_1) + b(y - y_1) + c(z - z_1) = 0 \tag{14}$$

This equation can be re-written in a general form as:

$$ax + by + cz + d = 0 \tag{15}$$

where

$a = (y_2 - y_1)(z_3 - z_1) - (y_3 - y_1)(z_2 - z_1), b = (y_2 - y_1)(z_3 - z_1) - (y_3 - y_1)(z_2 - z_1),\ c = (x_2 - x_1)(y_3 - y_1) - (x_3 - x_1)(y_2 - y_1)$ and $d = -ax_1 - by_1 - cz_1$.

By default, the normal distance should be equal or greater than the radius of the virtual sphere, i.e.

$$|r_n| \geq r_0 = 0.5d_2 \quad (16)$$

b) As can be seen from Fig. 8, for a candidate base element "k", only the surfaces of adjacent polytopes that are likely to bound the virtual sphere should be checked. Checking against unrelated surfaces of polytopes not only waste the computing time, but may result in false rejection of a valid base element because of not meeting the normal distance criterion to these irrelevant surfaces.

To identify the surfaces of polytopes that need checking, we propose to define a proximity spherical region $S(k)$ surrounding the base element under consideration. The spherical region is drawn from the candidate base element with an enlarged radius equal to two times of that of the virtual sphere, i.e. $r_1 = 2r_0 = d_2$. A surface whose centroidal distance to the base element falls within the spherical domain $S(k)$ is considered as a relevant surface and will subsequently be checked, otherwise the surface is considered to be outside the region of interest and will not be checked. Surfaces identified as within the proximity region will be stored in an array called $SurDom(k,j)$ , where $k$ is the order number of the spherical domain and $j$ is the serial number of the surfaces within the spherical domain.

All surfaces stored in $SurDom(k,j)$ are checked with respect to the normal distance criterion for the validation of the base element. The default criterion has been expressed in Eq. (16). If the distances from the base element to all these surfaces satisfy the criteria, the base element is valid. Otherwise additional checks will be warranted, as explained next.

c) If the above normal distance check fails for a particular surface, another layer of check is entered into operation to ensure that the surface is not one that is only marginally related to the base element, such as "e" and "f" in Fig. 8. As schematically shown in the figure, "e" and "f" have been identified to be within the proximity sphere, but they are not "facing" the base element and therefore checking for the normal distance criterion is not reasonable and could result in rejection of a valid base element such as element "k" shown in the figure.

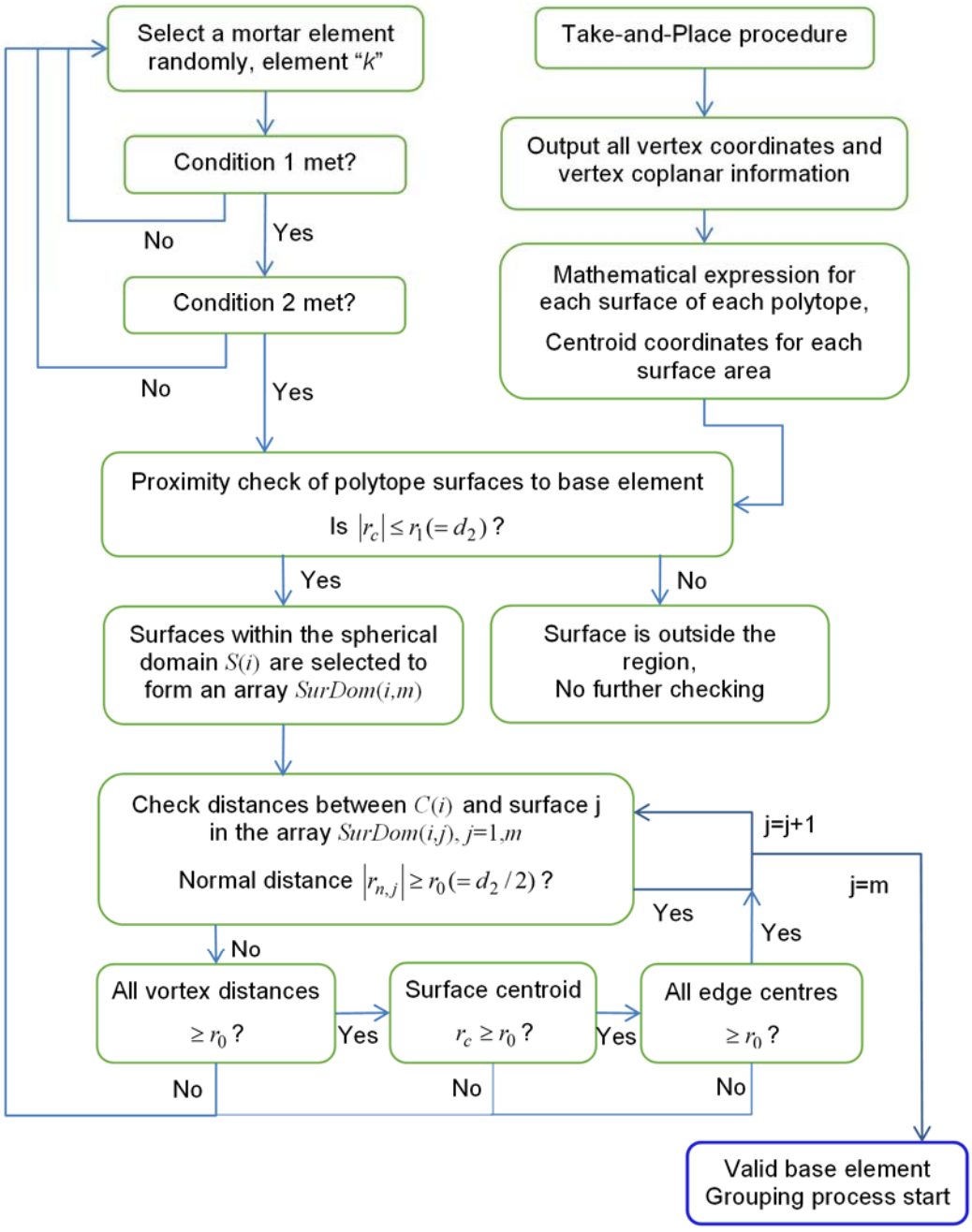


Fig. 9. Flowchart for selection of a base element for a supplementary aggregate

For simplicity, the following additional checks are carried out in conjunction with the normal distance check, such that when a normal distance check to a surface fails, the base element will be rejected only if any of the following conditions is met:

i) the distance from the base element to any vertex point of the surface is smaller than the specific limit, which by default will be $r_0$. (Otherwise the virtual sphere will surely intersect with the surface)

ii) the distance from the base element to the centroid of the surface is smaller than $r_0$, and

iii) the distance to the middle point of any edge of the surface is smaller than the specific limit, which by default is also taken as $r_0$.

Conditions ii) and iii) above are designed to cater for the extreme situation where the size of the current virtual sphere is considerably smaller than the size of the surface being checked against; in such a situation passing the vertex points check may not guarantee that there is sufficient space between the base element and the surface.

A special case worth noting is that there may be no element in the array $SurDom(k, j)$ for a candidate base element. This means the candidate base element is at least $d_2$ distance away from the centroid point of any surface in any existing polytope. Therefore this base element can be directly progressed as a valid base element without further checking.

The flowchart for the validation of a base element is shown in Fig. 9.

### *3.2.2. Grouping process*

After successfully selecting a valid base element, the next step is to create a new aggregate by grouping the mortar elements within the virtual sphere. The aggregate grouping process and the corresponding ITZ layer identifying process can be carried out simultaneously in this step. The procedure is as follows:

1. A mortar element is taken and checked. If all the four nodes of the mortar element are within the virtual sphere, the element is attributed the aggregate property and thus clustered into the new aggregate.
2. On the contrary, if none of the nodes of the mortar element is within the virtual sphere, the element remains as mortar and retains its mortar material property.
3. If some of nodes of a mortar element are within the virtual sphere while the remaining nodes are not, then the element is crossing the interface element and is given the equivalent ITZ property.

It should be noted that because only the remaining "mortar" elements are involved in the generation process for the supplementary aggregates, the new ITZ elements created for each new aggregate will have no conflict with and are different from the ITZ elements created in the primary stage in Section 3.1.

It should also be pointed out that because the space remaining for grouping is highly irregular and unstructured, some clusters formed in this way may not have the required volume to fall within the targeted size segment. To eliminate such clusters an equivalent volume check is included to judge the validity of the cluster to become an aggregate. For simplicity the critical volume is defined as the volume of the smallest sphere within the size segment, i.e. $Vol_{cr} = 4\pi(d_1/2)^3/3$ in the aggregate size segment of $[d_1, d_2]$.

The volume of each newly generated aggregate through the above grouping procedure can be obtained by adding all elements included in the cluster. The volume of an individual element can be calculated from the coordinates of all nodes of the element which can be directly output after the FE meshing. In the present mesoscale model tetrahedron element is used to mesh the 3D mesoscale structure. Let the coordinates of the four nodes of a tetrahedron element be $N_1(x_1, y_1, z_1)$, $N_2(x_2, y_2, z_2)$, $N_3(x_3, y_3, z_3)$ and $N_4(x_4, y_4, z_4)$, respectively, the volume of the element can be calculated by the standard expression:

$$Vol = \begin{vmatrix} 1 & 1 & 1 & 1 \\ x_1 & x_2 & x_3 & x_4 \\ y_1 & y_2 & y_3 & y_4 \\ z_1 & z_2 & z_3 & z_4 \end{vmatrix} \tag{17}$$

The grouping cluster can be considered as a valid secondary aggregate only when its volume is no smaller than a nominal volume for the size range to which the new aggregate is supposed to belong. Otherwise the cluster would be discarded and the procedure will repeat from the very beginning where a new base element candidate is selected by random from the mortar domain. In this way the new aggregates generated here can be made to follow exactly the target size distribution.

Fig. 10 shows the generation results of supplementary aggregates. It can be observed that all these aggregates are in reasonable gross shapes, although local irregularities exist as a result of grouping neighbouring mortar elements. Considering that the aggregates generated in this process are supplementary to the primary aggregates generated from the take-and-place procedure, the local irregularities are deemed to have only secondary effect, and hence are not further treated in the present study.

The final meso-structure can be determined subsequently after generating all the aggregates and identifying the corresponding ITZ layers, shown in Fig. 11. Comparing to Fig. 6 where only the primary aggregates from the take-and-place procedure are shown, the increased packing density due to the addition of the supplementary aggregates is remarkable.

Fig. 10. Supplementary aggregates (3D isometric view)

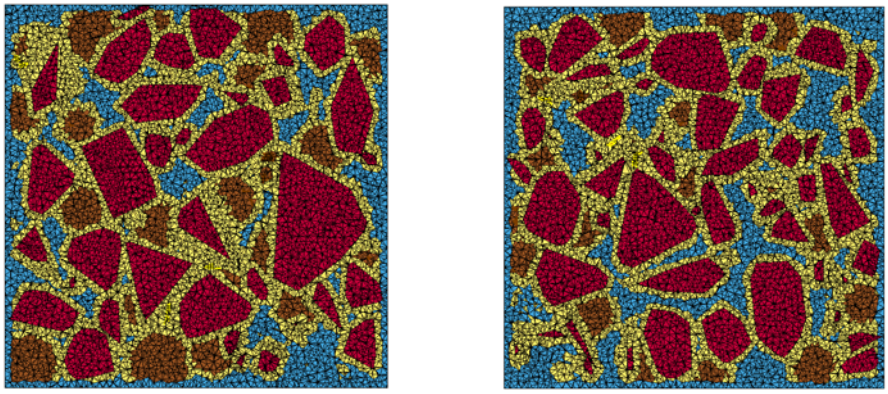

x = 20 cut plane view  x = 40 cut plane view

Fig. 11. Typical section views of final meso-structure of concrete (darker-brown colour aggregates are supplementary)

## 4. FE analysis of general behavior of concrete using the mesoscale model

In this section, the procedure described in Section 3 is implemented to create a complete 3D mesoscale model representing a typical type of concrete. Verification of the 3D mesoscale model is then presented, and this is followed by the application of the model to simulate the behaviour of concrete under various loading conditions. The underlying meso-mechanical damage process will be examined and discussed.

### 4.1 Outline of the 3D mesoscale model creation procedure

As described in detail in Section 3, the creation of a 3D mesoscale model is carried out in the following main steps:

1) Define the geometric space within which the mesoscale model will be created. For example, in the present study a cube with dimension size 50 mm is employed.
2) Creation of the primary mesoscale structure by the "Take and Place" procedure as described in Section 2. Herein this procedure is implemented by an in-house MATLAB code.
3) Finite element meshing for aggregates and the mortar matrix. Herein the software TETGEN [31] is used but this is not restrictive.
4) Generation of supplementary aggregates with the procedure as described in Section 3.2. The procedure is also implemented by an in-house MATLAB code.
5) Identification of the ITZ elements, also implemented with in-house MATLAB code.
6) Assignment of the material properties for the three types of elements, namely mortar matrix, ITZ and aggregates.
7) Conducting finite element analysis under a specified boundary and loading scenario using a general purpose FE solver. Herein LS-Dyna is employed [34].

## 4.2. Material model and material parameters

Under a general loading condition, damage and the nonlinear behaviour in concrete occur primarily in the mortar matrix and along ITZ. Therefore adequate nonlinear material models need to be considered for these two parts in order to represent the underlying damage process. At this juncture, it should be noted that the constitutive behaviour of quasi-brittle geomaterials like concrete bears similarities, and many 'geomaterial' models are designed to suit a range of such materials. Furthermore, because of the regularisation effect of the mesoscale structure, the sensitivity of the macroscopic behaviour of concrete in a mesoscale model to the choice of individual material description tends to be largely reduced and so the selection of the specific material model becomes less important, so long as the key properties, chiefly the elastic modulus and strength, are representative of the different component phases.

The material model employed for the mortar and ITZ parts in the present study is the K&C Concrete Damage Model. This material model is capable of describing the material failure due to tension, shear, as well as compression under various stress conditions, and it also includes pressure and strain rate dependent features. The detailed technical information about this material model can be found in [35]. The material model has been tested extensively and is found to be a suitable candidate for quasi-static as well as dynamic applications of concrete-like materials [36].

For normal concrete, the coarse aggregates are usually of much higher strength than the mortar matrix. It is reasonable to use a linear elastic material model for aggregates under low rate loadings. However for high dynamic loading such as shock and blast, the rapid propagation of stress wave could result in high stresses being developed in aggregates in a very different way as compared to low rate loading conditions, and this could subject the aggregates to potential failure [37]. Under this circumstance, a nonlinear material model becomes necessary. Herein we also use the concrete damage model for aggregates with however a failure strength matching that of the chosen aggregate type.

Table 1. Material parameters

| Component | Compressive strength (MPa) | Density (kg/m$^3$) | Poisson's ratio |
|---|---|---|---|
| Aggregate | 150 | 2600 | 0.23 |
| Mortar | 35 | 2000 | 0.2 |
| ITZ | 17.5 | 2000 | 0.2 |

Normal concrete of grade 30 MPa in cubic compressive strength is analysed using the mesoscale model. For this grade of concrete, the standard strength of mortar is around 35 MPa with the Young's modulus around 22 GPa [2, 15]. The properties of the ITZ layer are difficult to determine precisely but it is generally known to be weaker and is about 50% of the strength of the mortar matrix. Since in the present model the ITZ is represented by a layer of solid elements, thus as mentioned in Section 3.1 the ITZ layer will have a thickness that depends on the mesh (element) size, and this calls upon some trial analysis for the determination of the equivalent ITZ properties. In the present mesoscale modelling study, the element size is generally on the order of one 10$^{th}$ of the nominal aggregate size. For such a thin layer of equivalent ITZ, it has been found that use of a reduced strength as 50% of the mortar strength is appropriate. The properties of aggregates can vary significantly depending on the types of the aggregates, and for crushed stones the Young's modulus is around 50-60 GPa [2, 37]. Considering natural crushed stones of a nominal strength of 150 MPa the Young's modulus is assumed to be 50 GPa according to CEB [38].

Table 1 summarises the material properties for mortar, ITZ and coarse aggregate for the 30 MPa concrete in the mesoscale model.

It should also be pointed out that in the concrete material model used (K&C model) a crack localisation band width $L_c$ is employed to control the mesh sensitivity of the softening stage of

the response, such that the total fracture energy over the $L_c$ band would be constant and equal to the physical material fracture energy $G_f$. The default value for $L_c$ is set at 25.4 mm, presuming a nominal aggregate size of 1/3 inch (8.5 mm) and a typical crack band of 3 times of the aggregate size. For models in which the element size ($h_c$) is smaller than this, $L_c$ should normally be set equal to $h_c$ if softening is certain to localise within one element band such as in simple tension, otherwise $L_c$ will be multiples of $h_c$ and the precise choice will be subject to empirical judgement. For the mesoscale model herein and under general loading (other than direct tension or shear) it has been found that $L_c = 12$ mm is adequate and this value is used in all compression analyses.

## 4.3. "Numerical experiment" setup

3D mesoscale model of a cube specimen is developed. The size of the cube is 50 mm, which is commonly used in dynamic testing of concrete samples and is also a suitable size for quasi-static testing with coarse aggregates in a size range of 4-12 mm. It is worth noting that the model may be regarded as representing a standard concrete cubic specimen of 150 mm by simply scaling up all dimensions by a factor of 3, including the aggregate size and the mesh grid.

For uniaxial loading, the cubic specimen is restrained at the bottom along the axial (vertical, z-axis) direction, while loading is applied from the top face in the vertical direction. Other boundary conditions can be simulated by imposing different lateral constraints on the top and bottom faces; for instance a complete restraint in the lateral directions would simulate an upper bound friction condition at the loading and support faces. Specific confinement can also be simulated by imposing a given level of confining stress on the side faces.

In order to be able to produce the full range of the concrete response including the softening stage, the loading is applied in a displacement-controlled manner through imposing a velocity boundary condition. The transient analysis code LS-DYNA is employed to perform the analysis using an explicit time integration scheme. To minimise spurious oscillation in the simulation of quasi-static loading with an explicit transient analysis, the loading (velocity boundary) is made to follow a smoothed transition pattern. Controlling parameters that need to be specified in such a loading scheme include the rise time and the cap velocity. In a quasi-static analysis a rise time of at least 10 times of the fundamental period of the specimen is adopted and this generally ensures a negligible transient effect, whereas the velocity cap is chosen so that the specimen can be loaded to failure within an acceptable computing time. For dynamic loading,

the maximum velocity is dictated by the target nominal strain rate (velocity divided by the specimen length). More specific information about the velocity scheme will be given later for different loading conditions.

As stated before tetrahedral meshing is used in the present 3D mesoscale model to mesh the highly unstructured multi-layer domains. For tetrahedral mesh, several element formulations are available in general FE packages including LS-DYNA. Considering the fact that in the 3D mesoscale model the mesh is already considerably fine due to the need to mesh the mesoscale geometry, the 4-node tetrahedron element is employed after a mesh sensitivity study comparing the use of the 4-node and 10-node tetrahedron elements as well as the 8-node hexahedron element. In the final mesh setting, the length of the tetrahedron has a nominal size 0.5-1 mm, resulting in about 260k nodes and 158k elements respectively for the cubic model.

As a reference regarding the computation cost, the finite element simulations have been performed in a Linux system with 16 CPUs. As mentioned above the quasi-static analysis is carried out using an explicit time integration scheme and a longer duration is required to simulate a quasi-static response, thus the run time is relatively long and it can range between a few hours (for uniaxial tension) and a couple of days for compressions. Obviously for high rate dynamic loading, the run time would be drastically reduced, to the order of minutes.

## 4.4. Verification under quasi-static compression

The 3D mesoscale cubic specimen is examined firstly under a quasi-static compression. It is generally known that the compressive behaviour of a concrete specimen can be strongly influenced by the frictional constraint between the specimen and loading platen [39]. In the current 3D meoscale model, it is possible to simulate the varying friction force by incorporating a friction coefficient at the loading faces through a contact approach. For simplicity, two borderline scenarios are simulated herein; the lower bound is represented by a friction-free condition while the upper bound is represented by a complete lateral constraint on the top and bottom faces. The friction effect in typical laboratory tests should fall in-between the two borderline conditions.

To simulate a “quasi-static” compression, the velocity boundary condition was defined with a rise time of 4 ms and a velocity cap of 0.025 m/s following preliminary trial analyses. The computed axial stress - strain curves for the above mentioned lower and upper boundary conditions are shown in Fig. 12. A pair of experimental curves with “low” friction and “high”

friction are also shown in the figure for a comparison. Note that the grade of concrete in the experiment was not exactly 30 MPa so the absolute strengths are not to be compared in absolute terms.

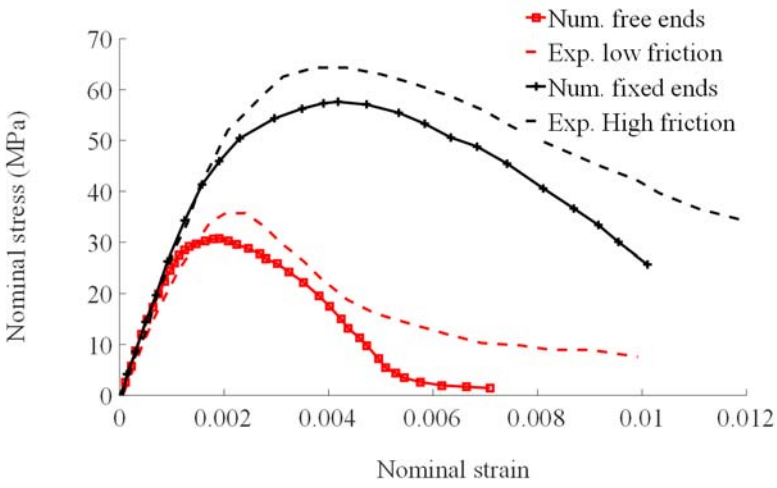


Fig. 12. Computed stress strain curves in comparison with typical experimental results [39]

As can be seen, the results from the mesoscale model show very good overall agreement with the experimental data in terms of elastic response (modulus), peak strains, and softening phase of the response. Both the computed and experimental results exhibit strong effect of the loading boundary conditions.

Fig. 13(a) and (b) show the damage patterns for low and high surface frictions respectively. The damage is represented by the plastic strain and this will be employed in similar damage illustrations hereinafter. As mentioned earlier, in the present simulation the concrete model (K&C) [35] is employed, and in this model three independent strength surfaces are defined for yield, maximum and residual strength respectively. At any stage the current damage state is defined as a linear interpolation between the maximum and either the yielding or residual failure surface, and the interpolation factor is a function of the modified effective plastic strain measure, $\lambda$, which is defined in the following form:

$$\lambda = \int_0^{\overline{\varepsilon_p}} \frac{\overline{d\varepsilon_p}}{r_f\left(1+\left(p+(p/r_f f_t)\right)\right)^{b_1}} \qquad \text{when } p \geq 0 \qquad (18a)$$

$$\lambda = \int_0^{\overline{\varepsilon_p}} \frac{\overline{d\varepsilon_p}}{r_f\left(1+\left(p+(p/r_f f_t)\right)\right)^{b_2}} \qquad \text{when } p < 0 \qquad (18b)$$

where $\overline{\varepsilon_p}$ is the effective plastic strain with the increment:

$$\overline{d\varepsilon_p} = \sqrt{\frac{2}{3} d\varepsilon_{ij}^p d\varepsilon_{ij}^p} \qquad (19)$$

$b_1$ and $b_2$ are damage scaling parameters for the case of the uniaxial compression and tension, respectively; $r_f$ is the dynamic increase factor that accounts for strain rate effect, $p$ is hydrostatic pressure and $f_t$ is the tensile strength of the concrete material.

Therefore, the plastic strain output from the model represents directly the damage (cracking) pattern. It can be seen that both of the global damage and internal crack patterns agree well the experimental observations. Under a low friction condition (Fig. 13(a)) the specimen was effectively separated into a series of small columns by the formation of the major cracks almost parallel to the applied load, and the cracks appear to follow the weakest path along the ITZ. On the other hand, under high friction (Fig. 13(b)) significant confinement develops in the triangular (cone-shaped) zones near the end faces, this lead to the well-known "hour glass" failure mode. Besides, the damage patterns appear to follow closely the weakest links formed by the ITZ around the aggregates (note that the shapes of aggregates are not shown in the contours to avoid confusion with the damage lines).

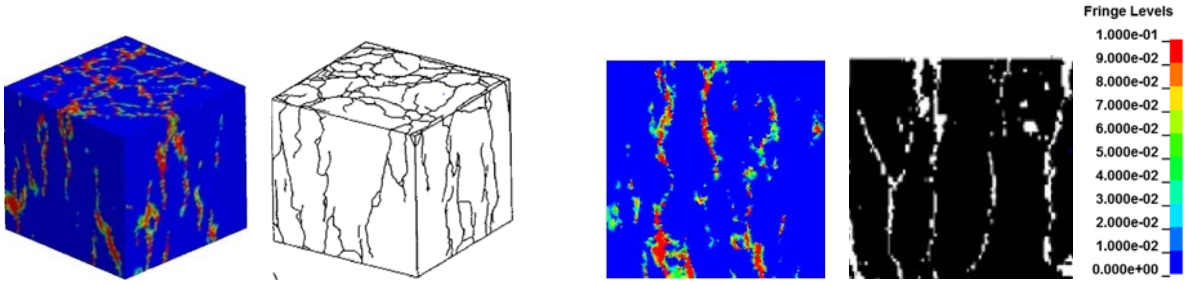


3D view Internal (section) view

(a) Lower loading-face friction

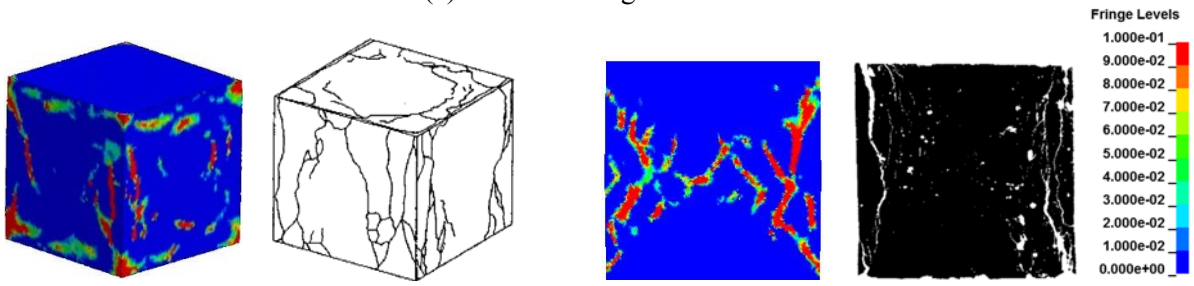


3D view Internal (section) view

(b) Higher loading-face friction

Fig. 13. Comparison of damage patterns between numerical results (left in each pair of graphs) and experimental observations (right, after [40])

## 4.5. Verification under quasi-static tension

In this section, the 3D mesoscale model is used to analyse the behaviour of concrete under uniaxial tension. The same material property parameters as in the compression analysis are used. The velocity loading boundary condition is applied directly on the top face in the same fashion as the compression loading. No lateral constraint (friction) is considered in the simulation of tension. The loading scheme used in the tension case is also similar to that used in the compression analysis with the same rise time, but the cap velocity was reduced 0.0025 m/s to reflect the fact that the tensile failure strain is about an order of magnitude smaller than the compressive failure strain. It is worth noting here that the exact loading rate is not important in the "quasi-static" analysis, so long as it avoids any sensible transient effect.

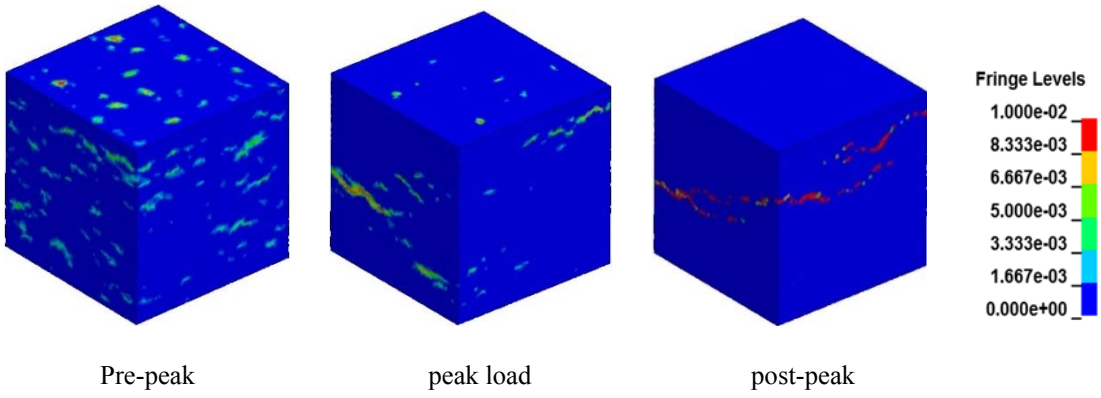


Fig. 14. Development of crack patterns

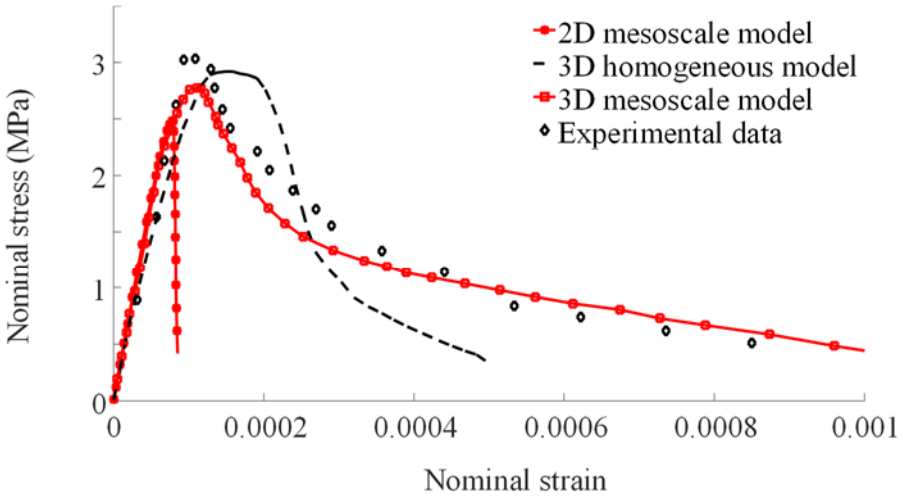


Fig. 15. Computed nominal stress-strain curve under direct tension (experimental data after [41])

Fig. 14 depicts a typical simulated fracture process of concrete under uniaxial tension. The corresponding tensile stress-strain curve is given in Fig. 15. It can be observed that upon the peak stress many micro-cracks developed and are mostly around the interface zone between mortar and aggregates. As the strain increases, some micro-cracks gradually coalesce to form macro cracks while other micro-cracks stop opening further. As the deformation continues, localization which is a well-known phenomenon in tension can be observed clearly from the 3D mesoscale simulation.

The direct tensile strength obtained in 3D mesoscale model is around 2.7 MPa, which is reasonable for the 30-MPa concrete under consideration. The strain at peak strength is around $1.2\times 10^{-4}$ which also agrees well with many experimental observations [41, 42]. Here if we also compare the results with the ones computed from 2D mesoscale model in [2], the 3D model again produces more reliable results than 2D model; in the 2D analysis the strain around peak load is much lower than the expected value. The relative lower strains at peak loads under both compression and tension indicate that 2D mesoscale model lacks the ability to produce realistic stress and strain states in concrete specimen. As for result from the 3D homogeneous model, it seems the softening part after peak load is too brittle. This could be attributed to the fact that the homogeneous model fails to predict a realistic path of crack propagation. As can also be seen from Fig. 14, some well-known fracture mechanisms such as crack deflection, crack branching and bridging can be well observed from the 3D mesoscale model.

### 4.6. Analysis of confined compression

The compressive behaviour of concrete is known to be sensitive to the lateral confinements. Generally speaking, with the increase of lateral confinement pressure, both the compressive strength and the ductility tend to show significant enhancement [43-45].

The 3D mesoscale model is tested under confined compression. Several levels of confining stress are considered in the simulation, namely 1.5, 4.5, 9 and 30 MPa. The confinement pressure is applied as lateral force on the side faces of the specimen, while the axial loading is still controlled by the velocity boundary condition with the same loading history as used in the uniaxial compressive analysis . With the explicit analysis scheme, the lateral confinement pressure is applied gradually in order to minimize spurious oscillations.

The axial stress - strain responses of the specimen at different levels of the confining pressure are presented in Fig. 16. As expected the compressive strength of the concrete increases

markedly with the increase of the confining pressure. Under relatively low confining pressure, the axial stress-strain curves exhibit well-defined peaks and clear softening branches. Both the peak strength and the ductility increase persistently with the increase in the confining pressure. Under further increased confinement, the post-peak branch turns to be flat and eventually exhibits a hardening stage. The transition from post-peak softening to hardening, i.e. the compressive behaviour of concrete specimen changes from quasi-brittle to apparently ductile, happens with a confining pressure of the order of 9 MPa. This phenomenon echoes very well the observations from other studies [44, 45]. A comparison with the experimental data from [45] is also given in Fig. 16. A good agreement can be observed in general. It is noted that at a high level of confinement with a pressure of 30 MPa, the numerical result appears to overestimate the confined strength, especially in the early nonlinear stage. This may be related to the fact that the experimental specimens were cylinders (150 mm in diameter and 300 mm in length) whereas the 3D mesoscale model is a cube of 50 mm (or 150mm cube by scaling). Nevertheless a good agreement in the overall comparison is evident.

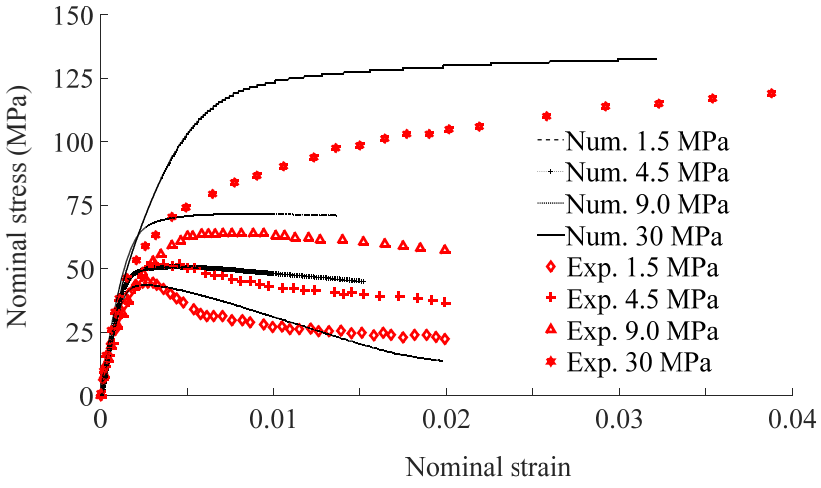


Fig. 16. Axial stress strain response under different levels of confining pressures (experimental data after [45]).

Fig. 17 shows damage patterns from the 3D mesoscale model. As can be seen, the failure crack patterns for different levels of confining pressures are different. In the lower confining pressure end, the macro-cracks at failure are nearly vertical (parallel to the axial compression), showing a splitting mode of failure. As the confining pressure increases, the damage (crack) zone becomes increasingly less oriented, and eventually turns into a crushing failure with well distributed fracture throughout the whole specimen. Experimental evidences (e.g. [46]) tend to

show a similar trend. Besides, the damage patterns appear to follow closely the weak links formed by the ITZ and extend into the mortar matrix.

From all of these comparisons, it is reasonable to say that the 3D mesoscale model has the capability to estimate the real stress strain state and the damage behaviour under various loading conditions with acceptable accuracy. Therefore a true 3D mesoscale model becomes a desirable solution to predict and better understand the failure mechanisms of concrete from micromechanical analysis. The model is further applied in the analysis of dynamic compression of concrete, which will be discussed in the Section 5.

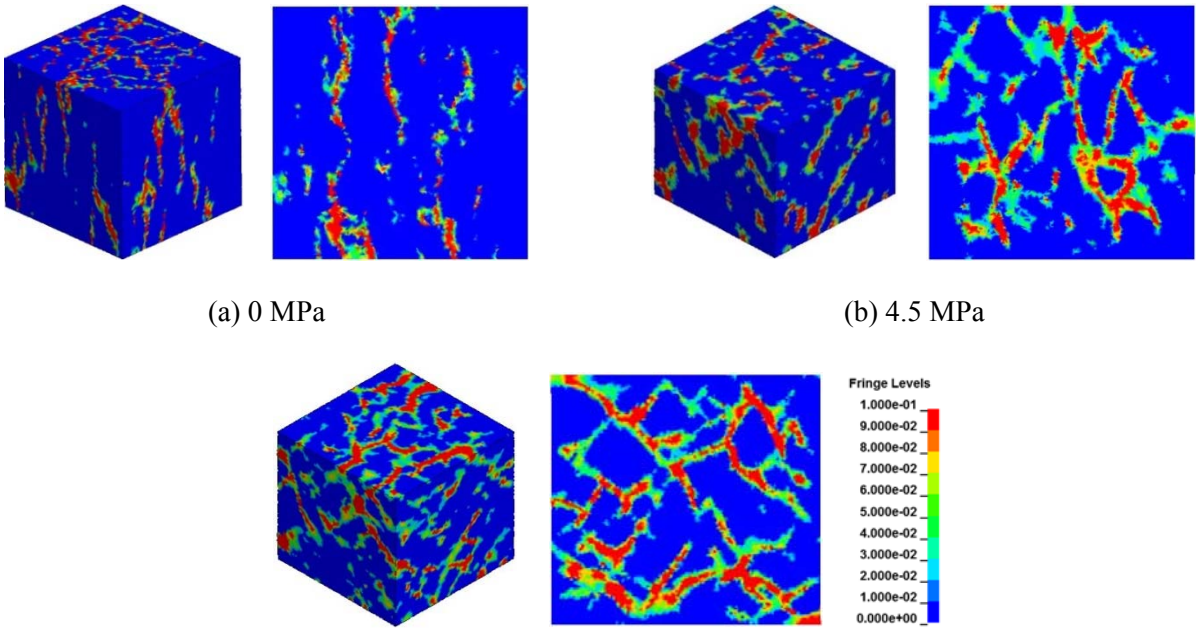


(a) 0 MPa (b) 4.5 MPa

(c) 30 MPa

Fig. 17. Global and internal damage patterns for different confining pressures

## 5. Application to dynamic compression

In this section the 3D mesoscale model is employed for a dynamic analysis of concrete under high strain rate compression. Experimental data generally suggests an apparent increase of the dynamic compressive strength with the increase of the strain rate, and a dynamic increase factor (DIF) is usually used in the engineering community to account for the strength enhancement due to high strain rates. However, the true mechanism underlying the occurrence of the DIF is still a subject of debate. As far as compression is concerned, a prevailing theory suggests that the DIF is largely attributed to the lateral inertial confinement (e.g. [47, 48]). More recent

numerical studies using 2D-type mesoscale models provide further support to this argument (e.g. [7, 49]) and also highlight possible contribution of the mesoscale heterogeneity towards the dynamic strength enhancement. However, a full representation of the mesoscale heterogeneity effect could only be achieved with a true 3D mesoscale.

The application of the present 3D mesoscale model to simulate the dynamic compression is straightforward. The dynamic loading is simulated by applying a velocity boundary condition in a similar way as in the quasi-static analysis, but with a high velocity in order to achieve a desirable strain rate. For example, the cap velocity is set at 2.5 m/s for a nominal strain rate 50 /s and 10 m/s for a nominal strain rate 200 /s in the 50-mm specimen. Note that in the dynamic simulation herein, no friction is considered at the loading face. To facilitate a direct observation of the contribution of the structural inertial effect, the constituent materials are considered to be rate insensitive, i.e., no embedded strain rate enhancement factor is adopted in the material properties in all the models. Thus any increase in the apparent compressive strength of the simulated test specimen is attributable only to the sample-wide dynamic effect, as well as the material heterogeneity. The apparent dynamic compressive strength is evaluated from the average peak stress on both the loading and supporting faces. For a comparison, a 2D homogeneous model, a 2D mesoscale model and a 3D homogeneous model are also analysed for the same variation range of the strain rates.

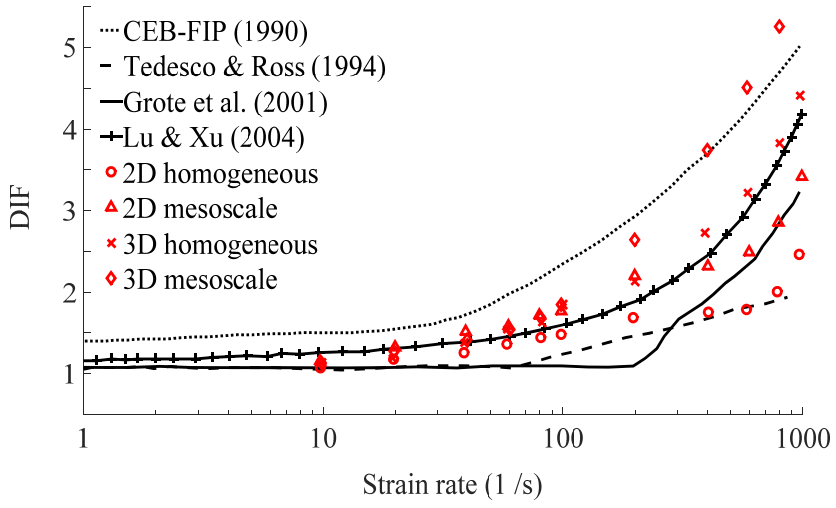


Fig. 18. Variation of compressive DIF with strain rate

Fig. 18 shows the variation of the predicted DIF with the strain rate from the simulations using the models mentioned above. Four empirical equations on DIF of concrete from the literature [37, 50-52] are also included for a comparison.

It is worth mentioning here that for dynamic compression test there is an upper limit of the strain rate concerning the stress and strain uniformity requirement upon the specimen reaching failure, and this strain limit is directly related to the length of the specimen. For 30-MPa concrete specimen of 50 mm in length a strain rate up to about 100 $s^{-1}$ is considered as acceptable [36]. Beyond this strain rate limit the peak stress at the loading and reaction ends may not be reached at the same time. A detailed discussion on such a phenomenon is beyond the scope of the present analysis. Herein for simplicity the apparent dynamic strength is evaluated as the average of the peak stresses at the loading and reaction ends, regardless whether they have been reached at the same time.

As can be observed from Fig. 18, all models exhibit an apparent increase in the compressive strength as the strain rate increases, despite that no strain rate enhancement has been incorporated in the material constitutive model. The general trend of the DIF curves in numerical models resemble well with the curves given by the empirical formulas. The 3D mesoscale model tends to predict the upper bound DIF among all numerical results, and this is deemed to be attributable to the enhanced contribution from the aggregates, as well as a fuller representation of the inertial confinement effect. Further comparison of the DIFs between 2D and 3D numerical models shows that the 2D numerical models markedly underestimate the DIF in the specimen, due apparently to an insufficient representation of the lateral inertial-induced confining effect in the third direction.

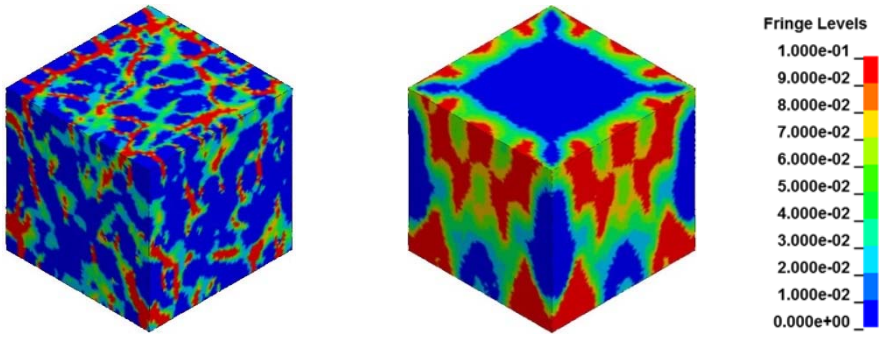


Fig. 19. Damege distribution at strain rate 200 /s (left: 3D mesoscale model; right: 3D homogeneous model)

The mesoscale heterogeneity is believed to contribute to the dynamic compression strength increase in two aspects, namely a) by promoting the distribution of damage (fracture) and thus better mobilising the strength of the specimen as a whole; this is evident from the damage

distributions in Fig. 19, and b) by having the stronger aggregates participate directly in the resistance, thus boost the overall stress level which then manifests as an increase of the apparent strength. This can be examined easily from the stress level achieved in the aggregates in the 3D mesoscale model. Fig. 20 shows the damage distributions in aggregates at the peak load stage for different strain rates. Note that damage only occurs in aggregates if the stress attained the "yield" strength level of 150 MPa. It can be seen that damage in aggregates appears at a strain rate of 50 $s^{-1}$ and it becomes increasingly more significant as the strain rate further increases.

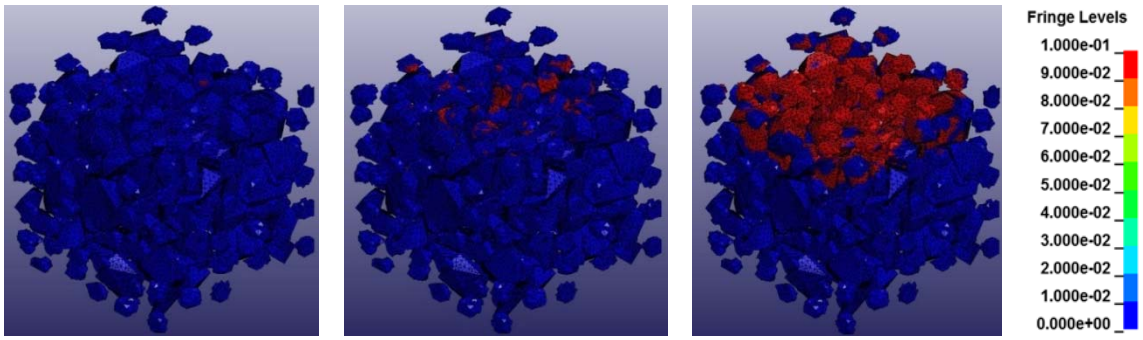


Strain rate 50 (1/s) Strain rate 200 (1/s) Strain rate 400 (1/s)

Fig. 20. Damage conditions of aggregates at peak load

## 6. Conclusions

A comprehensive procedure has been developed to generate realistic 3D mesoscale finite element model for concrete-like materials. The development has been catered to suit the needs of material investigation under general and complex stress conditions, including dynamic loading.

The mesoscopic geometric structure of a concrete specimen is generated in two steps. A take- and -place procedure is employed first to produce and pack convex polytopes as aggregates into a specimen space, which is a cube or prism in the present study. A fast detection of particle inclusion intersection procedure and a translate-and-rotate procedure are incorporated to enhance efficiency and effectiveness of the packing process. Finite element meshing is subsequently made using an efficient meshing code suitable for meshing the highly unstructured domains due to the existence of randomly shaped aggregate particles. The interface elements are formed by selecting an equivalent layer of elements surrounding the aggregate particles.

To tackle the shortcoming of the take-and-place procedure in terms of a limited packing density (in the range of 30-35%), an algorithm to identify and group suitable mortar elements into supplementary aggregates has been developed. The algorithm enables the supplementary aggregates to largely retain the randomness in the size and location of the aggregates, and at the same time fit to a desired grading curve.

The 3D mesoscale is verified in the simulation of the quasi static response of concrete under uniaxial compression, uniaxial tension, as well as confined compression. The simulated results resemble favourably the corresponding experimental observations.

The 3D mesoscale is also applied for simulation of the dynamic behaviour of concrete under high strain rate compression. Comparisons between the 3D mesoscale model and other modelling approaches demonstrate clearly the advantages of the 3D mesoscale model in terms of realistic representation of the stress field and the effect of the inertial confinement, as well as the participation of the aggregates in the dynamic resistance under high strain rates.

The procedure presented in this paper for the 3D mesoscale model is readily applicable for material investigation of concrete, with no restriction on aggregate sizes, shapes, and volumetric ratios, or loading and boundary conditions. The model allows investigations into the underlying concrete damage mechanisms under practically any loading and boundary condition, thus complement experimental testing and can lead to the development of more representative macroscopic concrete models for specific applications or improved mix design for enhanced material behaviour. The model can also be implemented in the analysis of a structural component where the stress conditions may be highly complicated. To control the computational cost in a structural component analysis it is possible to incorporate a two-scale approach such that the critical regions are modelled by the mesoscale model while the remaining regions by a homogenous model. As the 3D mesoscale model is developed in a continuum framework, interface between different scale regimes within the model domain is straightforward.

## Acknowledgements

The research reported in the paper is partly funded by the Chinese Scholarship Council and the University of Edinburgh through a joint scholarship for the PhD study of the first author.

## References


[1] Lu Y. Modelling the dynamic response of concrete with mesoscopic heterogeneity. In *Understanding the Tensile Properties of Concrete* (Ed. J Weerheijm), Chapter 8, Woodhead Publishing, 2013:218-267.

[2] Lu Y, Tu Z. Mesoscale modelling of concrete for static and dynamic response analysis-Part 2: Numerical investigations. Structural Engineering and Mechanics 2011;37:215-231.

[3] Grassl P, Grégoire D, Solano LR, Pijaudier-Cabot G. Meso-scale modelling of the size effect on the fracture process zone of concrete. International Journal of Solids and Structures 2012;49:1818-1827.

[4] Pedersen R, Simone A, Sluys L. Mesoscopic modeling and simulation of the dynamic tensile behavior of concrete. Cement and Concrete Research 2013;50:74-87.

[5] Tu Z, Lu Y. Mesoscale modelling of concrete for static and dynamic response analysis-Part 1: model development and implementation. Structural Engineering and Mechanics 2011;37:197-213.

[6] Wang Z, Kwan A, Chan H. Mesoscopic study of concrete I: generation of random aggregate structure and finite element mesh. Computers & Structures 1999;70:533-544.

[7] Zhou X, Hao H. Modelling of compressive behaviour of concrete-like materials at high strain rate. International Journal of Solids and Structures 2008;45:4648-4661.

[8] Mishnaevsky Jr L. Microstructural effects on damage in composites–computational analysis. Journal of Theoretical and Applied Mechanics 2006;44:533-552.

[9] Wriggers P, Moftah S. Mesoscale models for concrete: Homogenisation and damage behaviour. Finite elements in analysis and design 2006;42:623-636.

[10] Leite J, Slowik V, Mihashi H. Computer simulation of fracture processes of concrete using mesolevel models of lattice structures. Cement and concrete research 2004;34:1025-1033.

[11] Häfner S, Eckardt S, Luther T, Könke C. Mesoscale modeling of concrete: Geometry and numerics. Computers & structures 2006;84:450-461.

[12] Benkemoun N, Hautefeuille M, Colliat JB, Ibrahimbegovic A. Failure of heterogeneous materials: 3D meso-scale FE models with embedded discontinuities. International Journal for Numerical Methods in Engineering 2010;82:1671-1688.

[13] Caballero A, López C, Carol I. 3D meso-structural analysis of concrete specimens under uniaxial tension. Computer Methods in Applied Mechanics and Engineering 2006;195:7182-7195.

[14] Galindo-Torres S, Pedroso D, Williams D, Li L. Breaking processes in three-dimensional bonded granular materials with general shapes. Computer Physics Communications 2012;183:266-277.

[15] Nagai K, Sato Y, Ueda T. Mesoscopic simulation of failure of mortar and concrete by 3D RBSM. Journal of Advanced Concrete Technology 2005;3:385-402.

[16] Song Z, Lu Y. An algorithm for generation of 3D mesostructure of concrete for finite element analysis. 19th UK-ACME Conference, 2011.

[17] Wang X, Zhang M, Jivkov AP. Computational technology for analysis of 3D meso-structure effects on damage and failure of concrete. International Journal of Solids and Structures 2016;80:310-333.

[18] Yin A, Yang X, Zhang C, Zeng G, Yang Z. Three-dimensional heterogeneous fracture simulation of asphalt mixture under uniaxial tension with cohesive crack model. Construction and Building Materials 2015;76:103-117.

[19] Du C, Sun L, Jiang S, Ying Z. Numerical simulation of aggregate shapes of three-dimensional concrete and its applications. Journal of Aerospace Engineering 2011;26:515-527.
[20] Liu L, Shen D, Chen H, Xu W. Aggregate shape effect on the diffusivity of mortar: A 3D numerical investigation by random packing models of ellipsoidal particles and of convex polyhedral particles. Computers & Structures 2014;144:40-51.
[21] Huang Y, Yang Z, Ren W, Liu G, Zhang C. 3D meso-scale fracture modelling and validation of concrete based on in-situ X-ray Computed Tomography images using damage plasticity model. International Journal of Solids and Structures 2015;67:340-352.
[22] Man H-K, Van Mier J. Damage distribution and size effect in numerical concrete from lattice analyses. Cement and Concrete Composites 2011;33:867-880.
[23] Roubin E, Vallade A, Benkemoun N, Colliat J-B. Multi-scale failure of heterogeneous materials: A double kinematics enhancement for Embedded Finite Element Method. International Journal of Solids and Structures 2015;52:180-196.
[24] Skarżyński Ł, Tejchman J. Experimental Investigations of Fracture Process in Concrete by Means of X-ray Micro-computed Tomography. Strain 2016;52:26-45.
[25] Beddow JK, Meloy T. Testing and characterization of powders and fine particles. Heyden and Son Ltd, xxiii+ 195, 16 x 24 cm, illustrated, 1980 1980.
[26] Liu X, Garboczi E, Grigoriu M, Lu Y, Erdoğan ST. Spherical harmonic-based random fields based on real particle 3D data: improved numerical algorithm and quantitative comparison to real particles. Powder Technology 2011;207:78-86.
[27] De Berg M, Van Kreveld M, Overmars M, Schwarzkopf OC. Computational geometry: Springer; 2000.
[28] Ahn HT, Shashkov M. Geometric algorithms for 3D interface reconstruction. Proceedings of the 16th International Meshing Roundtable: Springer; 2008 405-422.
[29] Owen SJ. A Survey of Unstructured Mesh Generation Technology. IMR1998 239-267.
[30] Riedel W, Wicklein M, Thoma K. Shock properties of conventional and high strength concrete: Experimental and mesomechanical analysis. International Journal of Impact Engineering 2008;35:155-171.
[31] Si H. TetGen, a Delaunay-based quality tetrahedral mesh generator. ACM Transactions on Mathematical Software (TOMS) 2015;41:11.
[32] Shewchuk JR. General-dimensional constrained Delaunay and constrained regular triangulations, I: Combinatorial properties. Discrete & Computational Geometry 2008;39:580-637.
[33] Si H, Gärtner K. Meshing piecewise linear complexes by constrained Delaunay tetrahedralizations. Proceedings of the 14th international meshing roundtable: Springer; 2005 147-163.
[34] LS-DYNA. Keyword User's Manual. Livermore Software Technology Corporation, Livermore, California, 2012.
[35] Malvar L, Crawford J, Morrill K. K&C concrete material model release III–automated generation of material model input. Karagozian and Case Structural Engineers, Technical Report TR-99-243 2000.
[36] Tu Z, Lu Y. Evaluation of typical concrete material models used in hydrocodes for high dynamic response simulations. International Journal of Impact Engineering 2009; 36:132-146.
[37] Song Z, Lu Y. Mesoscopic analysis of concrete under excessively high strain rate compression and implications on interpretation of test data. International Journal of Impact Engineering 2012; 46:41-55.
[38] CEB-FIP Model Code 1990: Design of Concrete Structures. Thomas Telford; 1993.

[39] Van Vliet M, Van Mier J. Softening behaviour of concrete under uniaxial compression. Fracture mechanics of concrete structures 1995;1:383.
[40] Vonk RA. Softening of concrete loaded in compression: Technische Universiteit Eindhoven; 1992.
[41] Li Q, Ansari F. Mechanics of damage and constitutive relationships for high-strength concrete in triaxial compression. Journal of engineering mechanics 1999;125:1-10.
[42] Swaddiwudhipong S, Lu H-R, Wee T-H. Direct tension test and tensile strain capacity of concrete at early age. Cement and concrete research 2003;33:2077-2084.
[43] Imran I, Pantazopoulou S. Experimental study of plain concrete under triaxial stress. ACI Materials Journal-American Concrete Institute 1996;93:589-601.
[44] Papanikolaou VK, Kappos AJ. Confinement-sensitive plasticity constitutive model for concrete in triaxial compression. International Journal of Solids and Structures 2007;44:7021-7048.
[45] Sfer D, Carol I, Gettu R, Etse G. Study of the behavior of concrete under triaxial compression. Journal of Engineering Mechanics 2002;128:156-163.
[46] Rutland CA, Wang ML. The effects of confinement on the failure orientation in cementitious materials experimental observations. Cement and concrete composites 1997; 19:149-160.
[47] Donze F, Magnier S-A, Daudeville L, Mariotti C, Davenne L. Numerical study of compressive behavior of concrete at high strain rates. Journal of engineering mechanics 1999; 125:1154-1163.
[48] Li Q, Meng H. About the dynamic strength enhancement of concrete-like materials in a split Hopkinson pressure bar test. International Journal of solids and structures 2003;40:343-360.
[49] Lu Y, Song Z, Tu Z. Analysis of dynamic response of concrete using a mesoscale model incorporating 3D effects. International Journal of Protective Structures 2010; 1:197-217.
[50] Grote D, Park S, Zhou M. Dynamic behavior of concrete at high strain rates and pressures: I. experimental characterization. International Journal of Impact Engineering 2001;25:869-886.
[51] Lu Y, Xu K. Modelling of dynamic behaviour of concrete materials under blast loading. International Journal of Solids and Structures 2004;41:131-143.
[52] Tedesco J, Hughes M, Ross C. Numerical simulation of high strain rate concrete compression tests. Computers & structures 1994;51:65-77.